Supporting Information for

"Low porosity, high areal-capacity Prussian blue analogue electrodes enhance salt removal and thermodynamic efficiency in symmetric Faradaic deionization with automated fluid control"

Erik R. Reale,[a] Lyle Regenwetter,[a] Adreet Agrawal,[a] Brian Dardón,[a] Nicholas Dicola,[a] Sathvik Sanagala,[a] and Kyle C. Smith[a,b,c,d,*]

a. Department of Mechanical Science and Engineering, University of Illinois at Urbana-Champaign, Urbana IL, USA

b. Department of Materials Science and Engineering, University of Illinois at Urbana-Champaign, Urbana, IL, USA

c. Computational Science and Engineering Program, University of Illinois at Urbana-Champaign, Urbana, IL, USA

d. Beckman Institute for Advanced Science and Technology, University of Illinois at Urbana-Champaign, Urbana, IL, USA

*corresponding author's email: kcsmith@illinois.edu

Section S1: Design of the recirculating FDI system

Shown in Fig. S1 is the complete recirculating FDI system as a simplified diagram and as a computer rendering of the final design. Custom valves, which are low cost, low-volume alternatives to the off-the-shelf components, were designed to alternate flow to and from electrodes between brine and diluate reservoirs (Fig. S1, bottom left). Most notably, this approach enabled the use of flexible rubber tubing with an inner diameter of 0.8 mm, the smallest sold by Cole-Parmer, so as to minimize fluid volume within tubes in a manner that was compatible with the peristaltic pump that was used to induce flow (Masterflex L/X). To reduce mixing between diluate and brine streams, the fluid circuit was designed to minimize internal fluid volume as much as possible. Connections between the branching flow paths leading from both reservoirs to either electrode in the FDI cell were made using Y- and T-splitters manufactured by Cole-Parmer. Splitter connections have an internal volume of <10 μL, and an inner diameter of 1 mm to minimize diffusion across that cross-section. Compared to a previous iteration of the recirculating FDI system, which included a 3D-printed manifold through which water flowed into and away from the electrodes, redesigns removed extraneous volumes at its inlet and outlet.

Pinching of tubes was achieved by actuating servo motors. Initial testing determined that the amount of force required to seal the tubing by pinching was 70 N force and that a 2 mm actuation distance is sufficient. After testing such functionality and after surveying costs for different linear and rotational actuation mechanisms, 12 kg-cm torque servo motors were selected with a 180º motion profile operating at 5 VDC, allowing the valves to have a custom actuation angle. Creating an acceptable seal during valve switching required experimental tuning of servo actuation angles for each tube in each valve. Optimal angles were determined using a specialized Arduino code to iteratively increase the angle offset from the neutral position of the servo motors until an acceptable closure of the tube was attained. In this way, the optimum angle could be determined for future reference and coded into in the full recirculation cycle's control loop. In general, angles were determined to be approximately 40º from the neutral position for each servo motor. To test the operation of the full recirculation control loop, LEDs on the control board were used to display unique codes indicating the current control state of the system for ease of debugging. The valve components which held the tubing in place were 3D printed using stereolithography (SLA). During an early test checking for leaks and change in fluid flow, food dye was used as a visual indicator to confirm the effluent streams remained separated. During desalination tests, the controller was programmed to initiate valve switching via a trigger signal from the potentiostat (Biologic VMP-3).

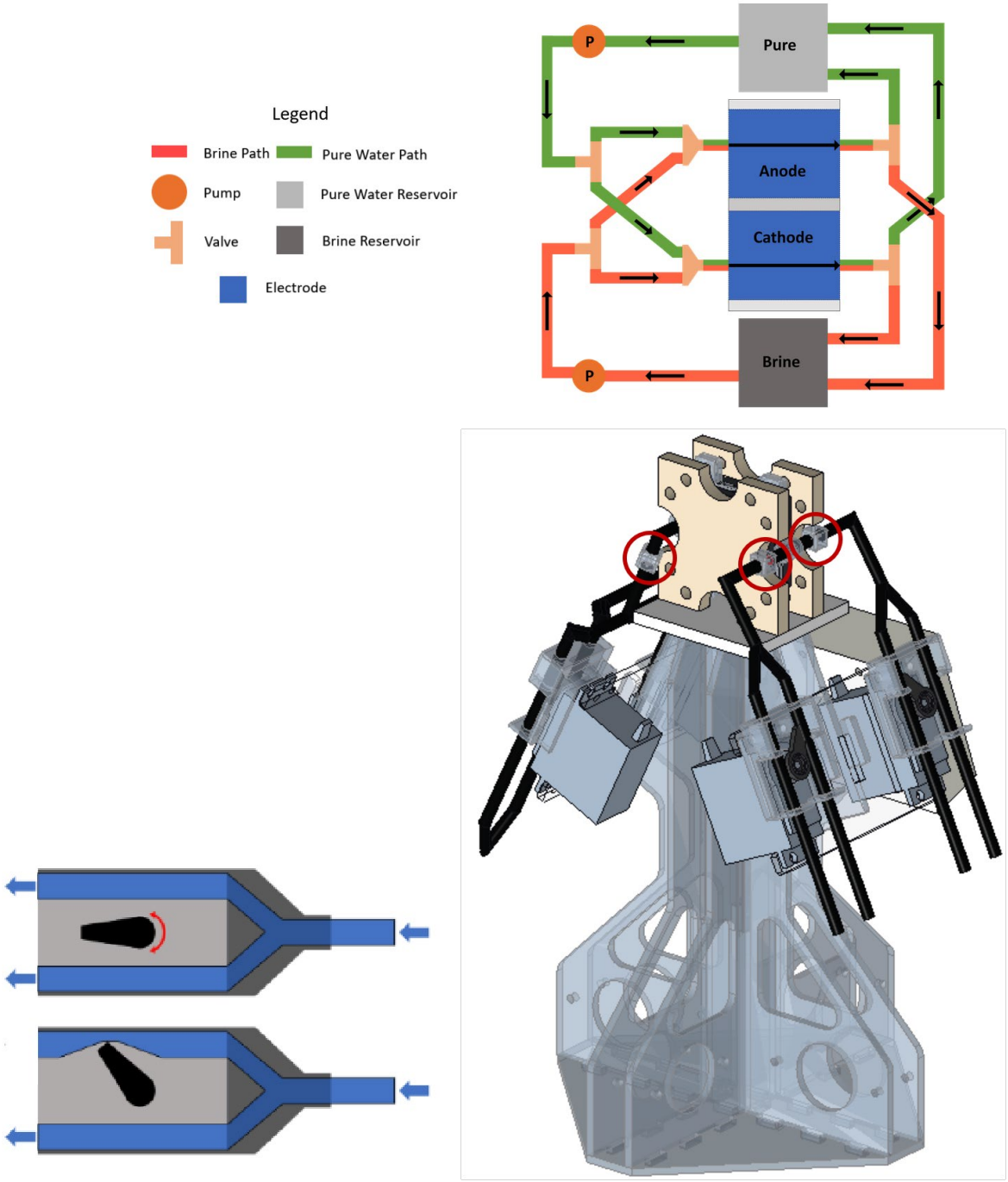

Figure S1: (Top) Simplified view of the FDI fluid recirculation system used. (Bottom left) Schematic representation of the custom-built valves used to actuate flow by pinching tubes using a rotor attached to a servo motor. (Bottom right) Computer-rendered view of the final recirculating system, including the core FDI cell, valves, fluid circuit, conductivity probes circled in red, and support stand. Not shown are the 5 mL reservoirs and the peristaltic pump. During the desalination process, a diluate stream and a brine stream are produced, flowing into their designated reservoirs.

To handle the power and control needs of the system, a compact electrical system was designed and fabricated. The key specifications were to power four servo motors running at 5 VDC, to control each such servo motors using a pulse-width modulated (PWM) signal, and to monitor an analog signal from the potentiostat to trigger valve-switching events. The system was implemented using an Arduino Uno R3 and a printed circuit board (PCB) containing a buck switching power converter to convert the 12 VDC input to 5 VDC and containing two power MOSFETs for pump control. A block diagram of the final electrical system and circuit board schematic is shown in Fig. S2. While in practice we used an independently controlled peristaltic pump, this circuit was originally designed to control two separate 12 VDC peristaltic pumps. In the schematic, J5 and SW1 are the plug and power switch. U1 and associated circuitry (C1-7, L1, etc.) constitute the buck switching power converter. Pump control MOSFETs Q1 and Q2 take as input signals Arduino digital outputs D5 and D6 into their gates, with both input signals tied to ground with 13 kΩ resistors R1 and R2. The pump connection header J2 connects to the 12 VDC input power though a Schottky diode D9 and to the drains of the Q1 and Q2 MOSFETs. The servo header J1 contains four 5 VDC pins, four ground pins, and 4 PWM signal pins from the Arduino. Input headers J3 and J4 take in analog input signals from the Biologic VMP-3 potentiostat. The seven LEDs are connected to Arduino digital outputs and pulled down to ground through 330 Ω resistors. The PCB layout was carefully designed to minimize the likelihood of RF interference affecting voltage conversion.

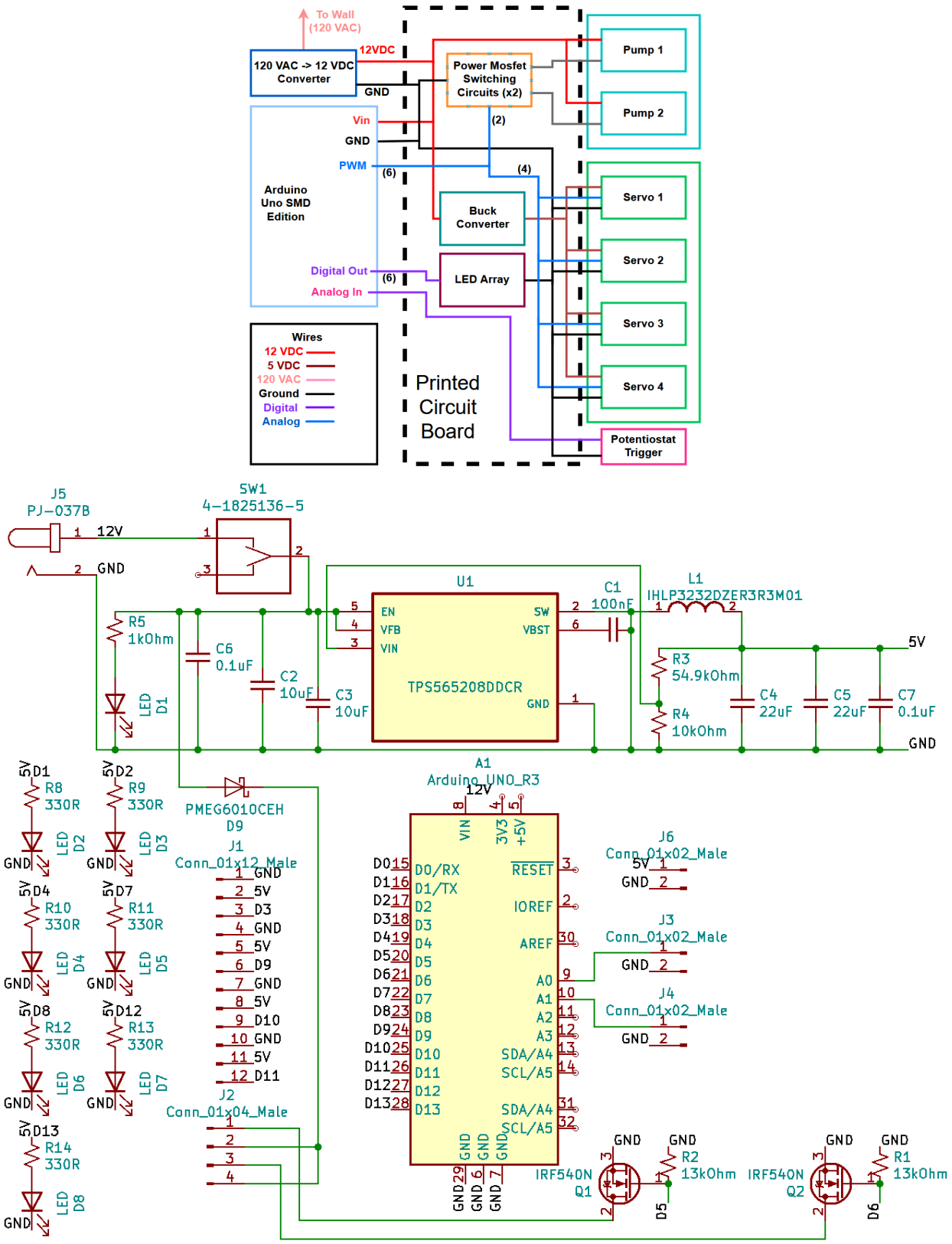

Figure S2: (Top) Block diagram of the electrical control system used to actuate valves in the recirculating FDI system. (Bottom) Electrical schematic of the printed circuit board (PCB) used.

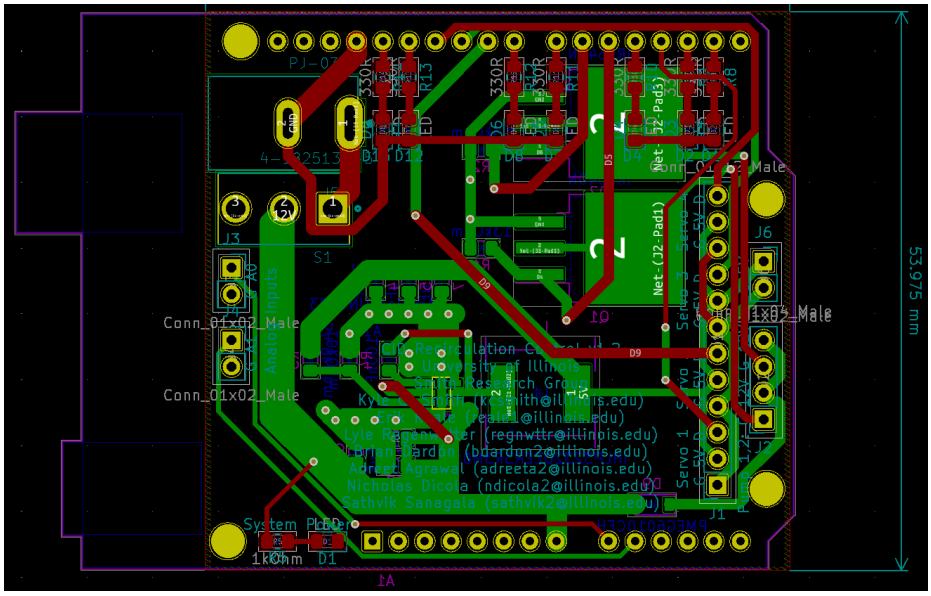
53.975 mm
Conn_01x02_Male
Conn_01x02_Male
Net-(J2-Pad1)
Net-(J2-Pad3)
Servo 1
Servo 2
Servo 3
Servo 4
Analog Inputs
System PCB
1kOhm
330R
J1
J2
J3
J4
J5
J6
S1
D1
D12
Kyle Reinhardt (regnwttr@illinois.edu)
Nicholas Dicola (ndicola2@illinois.edu)
Sathvik Sanagala (sathvik2@illinois.edu)

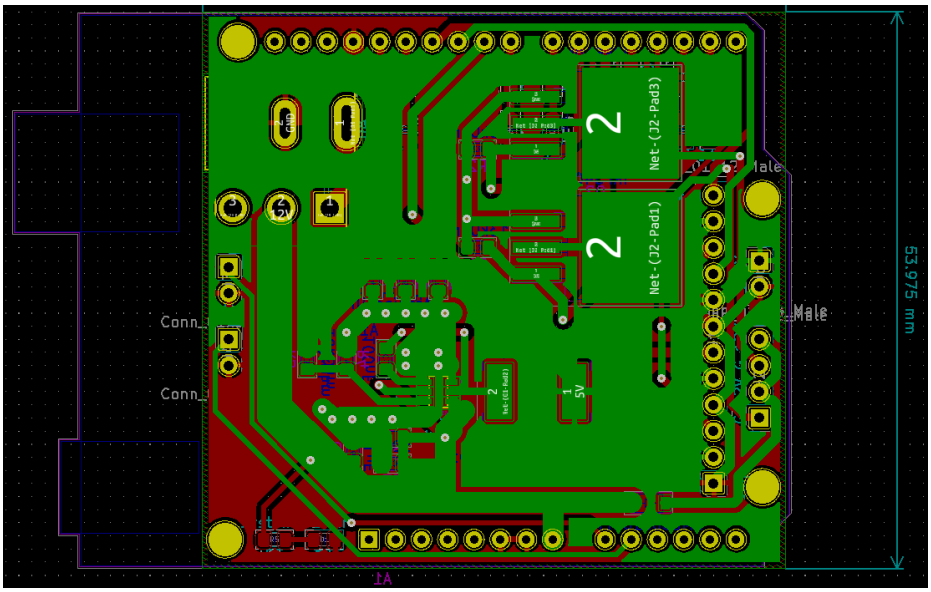
53.975 mm
Net-(J2-Pad3)
Net-(J2-Pad1)
5V

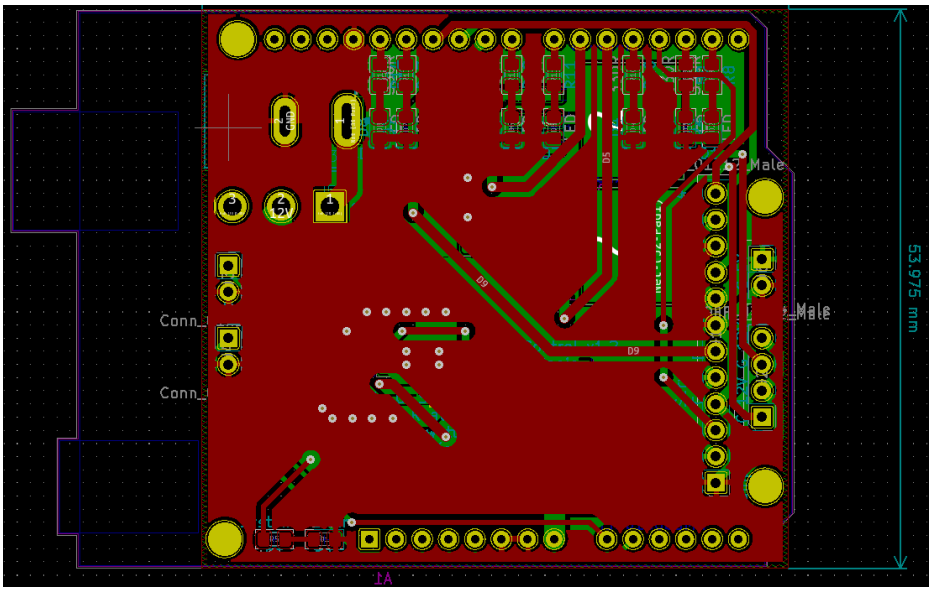

Figure S3: (top) Connection diagram of printed circuit board (PCB), (middle) back layer of PCB, and (bottom) front layer of PCB.

Section S2: Calibration of flow and valve timing events to minimize mixing between diluate and brine streams

Two 'pause periods' were introduced during the open-circuit phase of FDI cell cycling in order to independently time the valve actuation events for inlet and outlet valves, so as to minimize mixing of the diluate and brine streams. The first pause occurs between the start of the open-circuit period at the end of a given half-cycle and the switching of the inlet valves, allowing time for effluents to move from within the electrode to their appropriate reservoir. The second pause occurs between the events for switching of the inlet and outlet valves, and this pause provides time for brine and diluate streams to flow into the opposing side of the FDI cell from the previous half cycle. The valve actuation sequence of our experimental is also shown in Video S1. We found that, if all valves are switched simultaneously upon a given half-cycle's end, charge efficiency is reduced in proportion to the internal volume of the cell as a result of the brine and diluate within the electrodes and connective tubing flowing into their opposing reservoirs, undoing desalination progress. With electrode porosity and the internal dimensions of the fluidic circuit known, an effective internal volume of 87 μL was calculated for uncalendered 150 μm electrodes, resulting in that volume of fluid flowing into the wrong reservoir if such valve-actuation conditions were naively utilized.

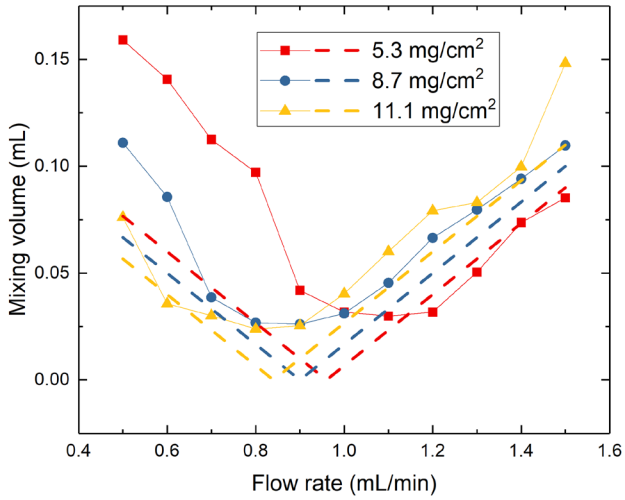

Figure S4: Curves used for calibrating the pause period in the three pairs of electrodes used in experiments, showing a minimum value for mixing volume. Dashed lines indicate ideal theoretical mixing in each pair of electrodes.

To overcome such limitations, we calibrated the timing of valve actuation events in the following way. The durations of the pause period between inlet and outlet valve actuations were calculated for each electrode pair by fixing the associated time delay to 10 s and subsequently characterizing the 'apparent mixing volume' when flowed at rates ranging between 0.5 to 1.5 mL/min. This apparent mixing volume was determined from an open-circuit FDI experiment beginning with one reservoir (1) containing water with an initial salt concentration $c_{b,1}$ of 100 mM and the other reservoir (2) containing deionized water with an initial salt concentration $c_{b,2}$ of 0 mM. The apparent mixing volume V_{mix} was calculated according to measured changes in the salt concentration $\delta c_1 = c_{b,1} - c_{a,1}$ of reservoir 1 before (b) and after (a) switching events by invoking mass conservation for salt: $V_{mix} = \delta c_1 V_{reservoir} / (c_{b,1} - c_{b,2})$. The flow rate that showed the least apparent mixing volume was used to find the pause period for 1 mL/min. For example, in Fig. S4, for the 5.3 mg/cm^2 electrode with a 10 second pause the flow rate with the least mixing was 1.1 mL/min. Accordingly, for an experiment using a flow rate of 1 mL/min the pause period was adjusted to 11 seconds in order to compensate for the longer residence time associated with a lower flow rate having the same mixing volume. The dashed lines in Fig. S4 show the degree of effluent mixing expected for an ideal flow ignoring any dispersion or diffusion effects at the interface between diluate and brine solutions, showing qualitative agreement with experimental measurements. Due to the reduction in porous volume, denser electrodes require shorter pause periods for a 1 mL/min flow and had lower mixing volumes, with deviations above or below the optimal choice increase the mixing volume.

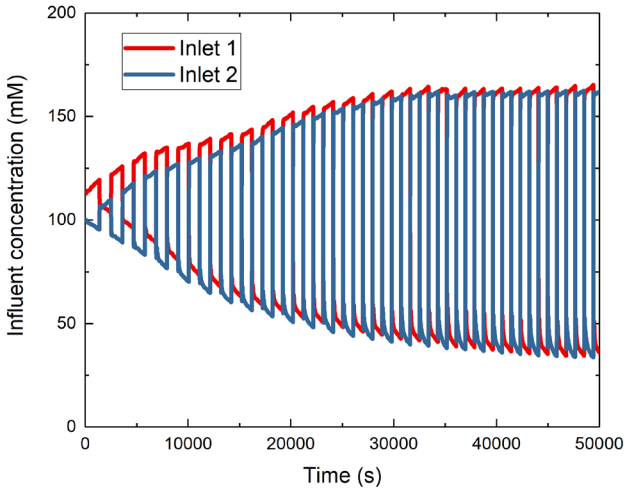

Figure S5: Salt removal measurements for 100 mM influent using the 150 µm, 5.3 mg/cm^2 electrode, showing alternating concentration at the two inlets as flow is redirected between half-cycles.

Fig. S5 shows the concentration at both inlets over time during desalination using the least dense electrodes. During initial cycles the concentration change is approximately linear with time at a rate, producing charge efficiencies of 85-95%. However, each subsequent cycle shows diminishing returns until reaching a maximum salt removal of approximately 65 mM.

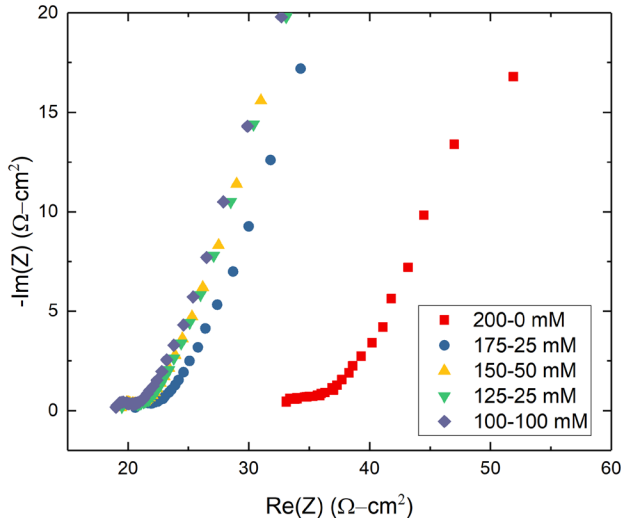

Figure S6: EIS data replicating varying degrees of desalination using the 5.3 mg/cm^2 electrode, ranging from both reservoirs containing the same concentration of saltwater up to complete desalination.

To confirm that the temporal increase in impedance during desalination seen in EIS data was a result of changes in concentration and ionic conductivity, a separate EIS experiment was performed with the 5.3 mg/cm^2 electrode. Rather than running EIS during a desalination experiment, the two reservoirs were filled with saltwater at specific concentrations to replicate increasing degrees of desalination. The first experiment was performed with both sides of the cell containing 100 mM saltwater. Then, the concentration difference increased to replicate intervals of 25 mM concentration reduction in the diluate, with the final experiment using deionized water and 200 mM brine. Similar to data in Fig. 7A, results in Fig. S6 show only a ~2 Ω-cm^2 increase in real impedance even when one half of the cell contained only 25 mM saltwater. There was an increase in real impedance of over 10 Ω-cm^2 when deionized water was flowed through one side of the cell, showing the steep rise in ionic resistance at high salt removal.

Section S3: Colloid-inspired electrode fabrication physics

When developing the modified wet-phase inversion (WPI) process, DLVO theory was employed to guide experimental process conditions based on how inter-particle forces were expected to change with bath properties. The DLVO theory can be used to predict the interparticle potential E_{ij} acting between two particles i and j separated by a distance x, including competing contributions from van der Waals and electrostatic forces (Goodwin, 2009):

$$E_{ij} = \left(64\pi\varepsilon D\left(\frac{k_B T}{e}\right)^2 tanh\left(\frac{e\zeta_i}{4k_B T}\right) tanh\left(\frac{e\zeta_j}{4k_B T}\right) e^{-x/\lambda_D} - \frac{A_{ij}}{6x}\right)\frac{R_i R_j}{R_i + R_j}$$

Here, we recognize the dependence of E_{ij} on particle radius R_i, particle zeta potential ζ_i, interparticle Hamaker constant A_{ij}, Debye length λ_D, dielectric permittivity ε of intervening solution, diffusivity of ions in solution D, and the thermal voltage $k_B T/e$. Within the electrode slurry, interactions between particles are governed by van der Waals and electrostatic forces, illustrated in Fig. S7A, in which active and conductive particles are suspended in a slurry surrounded by NMP solvent. These forces remain active during the solidification process as NMP is removed and replaced by water from the bath. The van der Waals force is always attractive, determined by the Hamaker constant A, the distance between particles x, and their respective radii R (Israelachvili, 2011). When both particles are immersed in a fluid with its own Hamaker constant (in this case a mixture of NMP and dissolved PVDF) the fluid reduces the overall attractive force between particles, an effect which can be approximated using the following equation $A_{ij} = \left(\sqrt{A_{ii}} - \sqrt{A_{solvent}}\right)\left(\sqrt{A_{jj}} - \sqrt{A_{solvent}}\right)$ (Israelachvili, 2011). The Al_2O_3 particles used presently as a surrogate material possess a Hamaker constant of 1.45x10^{-19} J in vacuum (Bergstrom, 1997),

while carbon black particles possess a value of 2.53×10^{-19} J (Dagastine et al., 2002), and the NMP solvent's Hamaker constant is 8.21×10^{-20} J (Zhu et al., 2011). It must be noted the latter value does not take the presence of the PVDF binder into account. The presence of solvent results in a Hamaker constant between the carbon black particles equal to 4.69×10^{-20} J and 2.04×10^{-20} J between the carbon black and Al_2O_3. Our experimental results suggest that the preferential van der Waals attraction between carbon black particles enables the aggregation of the carbon black network, rather than random Brownian motion which acts to disperse them, because carbon black particles are more attracted to each other than to the pseudo-active particles. However, electrostatic repulsion acts against this aggregation.

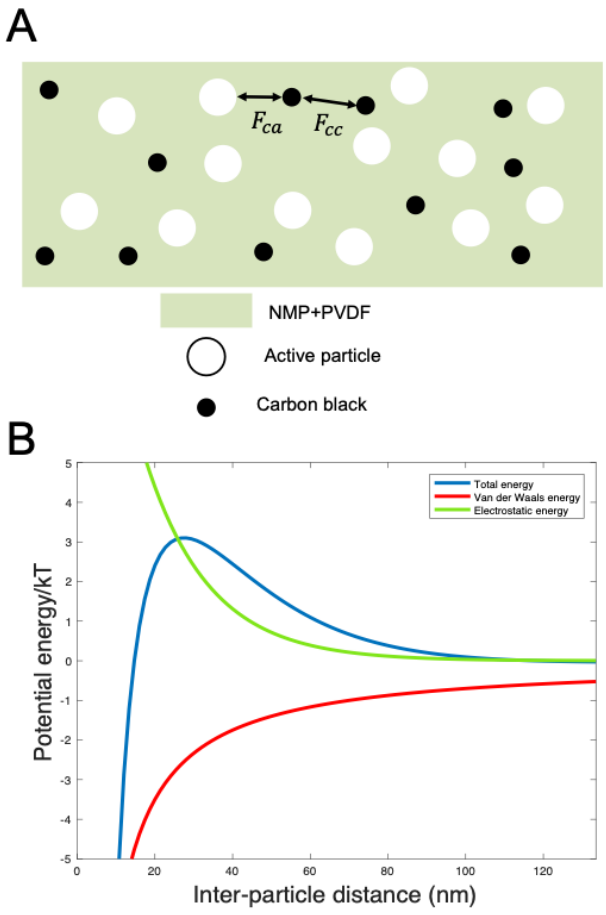

Figure S7: (A) Simplified depiction of active and conductive particles in a colloidal suspension where such particles are subjected to inter-particle forces. (B) Potential energy versus separation distance of two Al_2O_3 particles in NMP, normalized by thermal energy, based on the DLVO theory. This total potential energy is the sum of attractive van der Waals interactions and repulsive electrostatic energy shown as separate curves.

The electrostatic force between particles is a significant barrier to a carbon network forming, because all carbon particles have a negative zeta potential of -22 mV in DI water. These

interactions result in strong mutual repulsion between carbon particles. In the Al_2O_3 surrogate electrodes, the Al_2O_3 has a positive zeta potential of 24 mV at neutral pH, leading to the carbon particles being more attracted to the alumina than to each other. In the DLVO theory, this repulsion is quantified as a potential energy barrier which carbon particles must overcome, shown by the local maximum in combined potential energy plotted in Fig. S7B. Due to the dependence of the electrostatic and van der Waals forces on distance in Eq. 1, attractive van der Waals forces dominate at short distances. To aggregate, the carbon particles need either sufficient energy to overcome repulsion, such that electrostatic forces are weakened, or for the zeta potentials of carbon and active particles to possess the same sign, such that their driving forces for aggregation are suppressed.

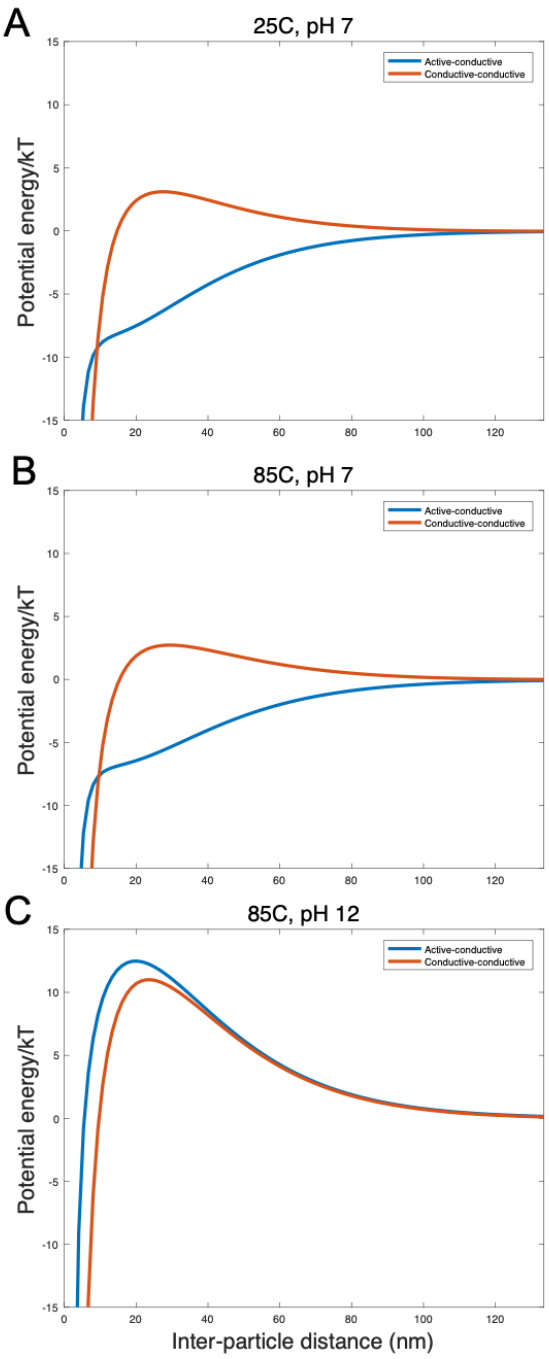

Figure S8: Theoretical potential energy curves for carbon and alumina particles in different baths. (A) DI water at room temperature, (B) DI water heated to 85°C, and (C) pH 12 water heated to 85°C.

The potential energy curves of three different baths are shown in Fig. S8, illustrating how increasing bath temperature and pH leads to the increase in conductivity shown in Fig. 2A-2C of the article's main text. By increasing bath temperature, the repulsive energy between conductive

carbon particles expected by the DLVO theory increases by only 8%, but the thermal energy of the particles in the slurry increases 28%, giving them more energy to overcome that repulsion to induce their aggregation. Then, when increasing pH, the zeta potential's magnitude increases, causing strengthened repulsion between carbon. However, the zeta potential of Al_2O_3 changes signs, repelling the carbon, and the repulsive energy between carbon and Al_2O_3 is greater than between two carbon particles. As a result, carbon particles prefer to aggregate with each other, rather than to aggregate with the other Al_2O_3 particles.

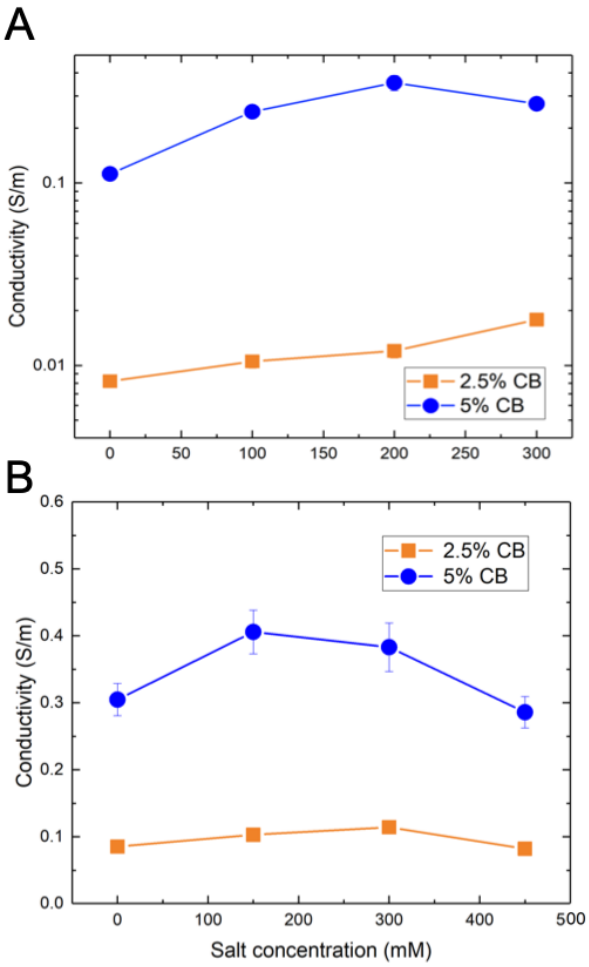

Figure S9: Conductivity for surrogate active electrodes immersed in saltwater at varying concentrations, either at (A) room temperature or (B) 85ºC.

In addition to the experiments with increasing bath temperature and pH reported in the main text, salt concentration of inversion baths was also increased with the expectation that the Debye length would be shortened, weakening electrostatic repulsion between carbon particles. Conductivity was shown to increase over its value for electrodes in DI water, though too much

salt caused conductivity to decline. This result is likely caused by carbon becoming so mutually attractive that it flocculates, rather than forming a branching network. Experiments combining high salt concentration and high pH were not attempted because their intended effects were thought to counteract each other on the basis of DLVO theory: salt weakens electrostatic forces while increasing pH strengthens it in a beneficial manner.

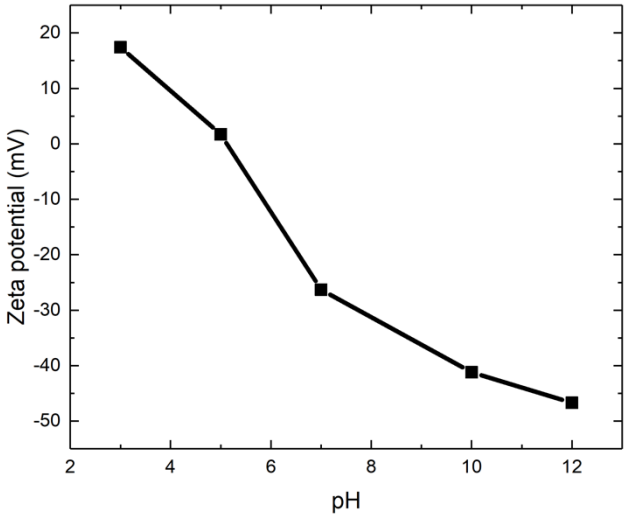

Figure S10: Zeta potential measurements for PBA particles dispersed in water at pH controlled by the addition of HCl or NaOH.

Figure S10 shows the variation of zeta potential with pH for PBA nanoparticles dispersed in water, measured using a Malvern zetasizer. Compared to carbon black zeta potential that decreases from to -24.5 to -40 mV over this pH range (Sis and Birinci, 2017), the zeta potential of PBA nanoparticles decreased from -26.3 to -46.7 mV. In an alkaline bath, the PBA nanoparticles therefore repel the carbon 2.7 times more strongly than at neutral pH, compared to the carbon particles repelling each other 2.5 times as strongly, a slight advantage which is likely responsible for preferential aggregation and the increased electronic conductivities that we observe for electrodes prepared by modified WPI.

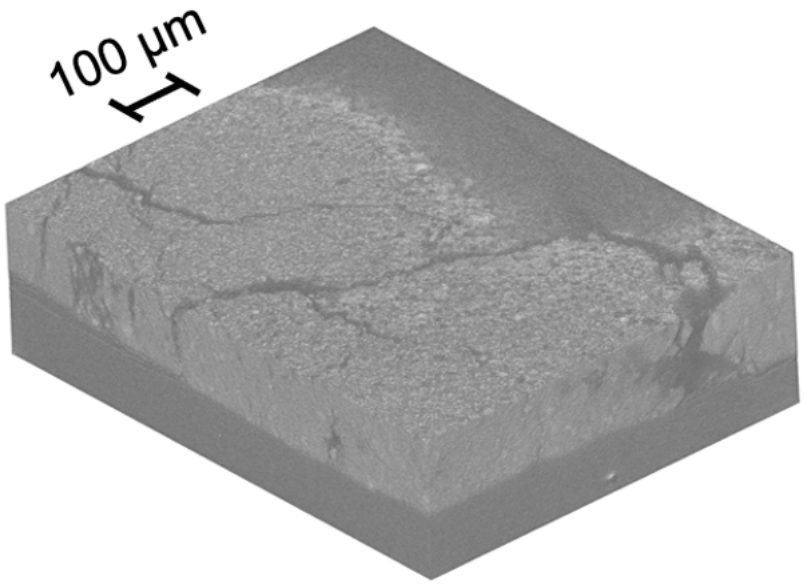

Figure S11: Complete X-ray CT image of a calendered PBA sample, showing fissures.

A larger view of the same electrode sample in Fig. 3E is showing in Fig. S11, also imaged using X-ray CT. Video S2 illustrates these features in three dimensions by scanning from the current collector surface through the thickness direction (z) of the electrode. The complete sample shows several microscopic fissures, believed to be formed by a lack of contact with the substrate, unlike macroscopic cracks formed by mechanical stresses during drying. Further examination reveals that such fissures extend, and subsequently narrow, from small aggregates (<10 µm) pinned at the electrode/graphite interface (Video S2), suggesting that such aggregates act to nucleate defective fissures and that their elimination in the future could further improve electrode homogeneity and function. Fissure formation beginning at the surface of the graphite foil substrate is visible Video S2, with voids becoming narrower as they extend upwards through the thickness of the electrode.

References

Bergstrom, L., 1997. Hamaker constants of inorganic materials Lennart. Adv. Colloid Interface Sci. 70, 125–169. https://doi.org/10.102/la201387d

Dagastine, R.R., Prieve, D.C., White, L.R., 2002. Calculations of van der Waals forces in 2-dimensionally anisotropic materials and its application to carbon black. J. Colloid Interface Sci. 249, 78–83. https://doi.org/10.1006/jcis.2002.8239

Goodwin, J., 2009. Colloids and Interfaces with Surfactants and Polymers, First. ed. Wiley.

Israelachvili, J.N., 2011. Intermolecular and Surface Forces, 3rd ed. Elsevier Inc.

Sis, H., Birinci, M., 2017. Effect of nonionic and ionic surfactants on zeta potential and dispersion properties of carbon black powders. Colloids Surfaces A Physicochem. Eng. Asp. https://doi.org/10.1016/j.colsurfa.2009.03.039

Zhu, M., Park, J., Sastry, A.M., 2011. Particle Interaction and Aggregation in Cathode Material of Li-Ion Batteries: A Numerical Study. J. Electrochem. Soc. 158, A1155. https://doi.org/10.1149/1.3625286